

# Soil Moisture Active/Passive (SMAP) L-Band Microwave Radiometer Post-Launch Calibration

Jinzheng Peng, Jeffrey R. Piepmeier, *Senior Member, IEEE*, Sidharth Misra, *Member, IEEE*,  
Emmanuel P. Dinnat, *Senior Member, IEEE*, Derek Hudson, David M. Le Vine, *Life Fellow, IEEE*,  
Giovanni De Amici, Priscilla N. Mohammed, *Member, IEEE*, Simon H. Yueh, *Fellow, IEEE*, Thomas  
Meissner, *Senior Member, IEEE*

**Abstract**— The SMAP microwave radiometer is a fully-polarimetric L-band radiometer flown on the SMAP satellite in a 6 AM/ 6 PM sun-synchronous orbit at 685 km altitude. Since April, 2015, the radiometer is under calibration and validation to assess the quality of the radiometer L1B data product. Calibration methods including the SMAP L1B TA2TB (from Antenna Temperature ( $T_A$ ) to the Earth's surface Brightness Temperature ( $T_B$ )) algorithm and TA forward models are outlined, and validation approaches to calibration stability/quality are described in this paper including future work. Results show that the current radiometer L1B data satisfies its requirements.

**Index Terms**—SMAP, Microwave Radiometer, Calibration, Validation, Simulation, Radiometry

## I. INTRODUCTION

SMAP is one of four first-tier missions recommended by the US National Research Council's Committee on Earth Science and Applications from Space (Earth Science and Applications from Space: National Imperatives for the Next Decade and Beyond, Space Studies Board, National Academies Press, 2007). The primary science objective of SMAP is to provide global maps of soil moisture every 2~3 days with an uncertainty of less than  $0.04 \text{ m}^3\text{m}^{-3}$ . The SMAP mission was designed to have complementary spaceborne L-band radar and radiometer instruments that share a rotating 6-m mesh reflector antenna (Entekhabi

et al., 2010). The mission's observatory was launched into a 685-km near sun-synchronous 6 AM/PM orbit on January 31, 2015.

The radar and radiometer provide simultaneous brightness temperature and backscatter measurements at spatial resolutions of about 3 and 40 km, respectively. Considering the relative sensitivity of the radar and radiometer measurements to soil moisture, surface roughness and vegetation scattering, the radar and radiometer measurements are designed to be combined to derive enhanced soil moisture mapping with a 10 km intermediate resolution. For the radiometer, this objective requires radiometric uncertainty of better than 1.3 K (with fore and aft observations averaging) with spatial resolution of approximately 40-km and geolocation accuracy of at least 4 km (Entekhabi et al., 2010). The SMAP mission high-level science requirements and derived instrument requirements related to the radiometer are shown in Table 1.

Table 1. SMAP Radiometer Science/Instrument Requirements.

Scientific Measurement Requirements	Instrument Functional Requirements
<u>Soil Moisture:</u> 0.04 m <sup>3</sup> m <sup>-3</sup> volumetric uncertainty (1- $\sigma$ ) in the top 5 cm for vegetation water content $\leq 5$ kg m <sup>-2</sup> ; Hydroclimatology at 40-km resolution	<u>L-Band Radiometer (1.41 GHz):</u> Polarization: V, H, T <sub>3</sub> and T <sub>4</sub> Resolution $\leq 40$ km Radiometric Uncertainty* $\leq 1.3$ K Constant 40° incidence angle**
Sample diurnal cycle at consistent time of day (6am/6pm Equator crossing); Global, 3-day (or better) revisit	Swath Width: 1000 km Minimize Faraday rotation
Observation over minimum of three annual cycles	Baseline three-year mission life
* Includes precision and calibration stability ** Defined without regard to local topographic variation	

SMAP's L-band radiometer was commissioned in March 2015 and as of June 2016 has been operational for more than a year. Early in its mission, SMAP provided 10-km resolution soil moisture globally every three days using a combined active-passive microwave instrument comprising an unfocused synthetic aperture radar (SAR) and a radiometer. In July the radar ceased transmissions and has remained in receive-only mode since. By itself the radiometer enables 40-km resolution soil moisture with the same three-day global coverage. Nonetheless, with its conical-scanning (real aperture) antenna and advanced RFI mitigation capabilities, the SMAP radiometer is providing high-quality brightness temperature measurements of Earth's land, ice and ocean surfaces.

The SMAP radiometer design presents unique calibration challenges and solutions. At L-band, emissions from unwanted sources such as the galaxy, Sun, Moon need to be removed (Wentz et al, 2012). The mesh reflector antenna used by SMAP presents a different calibration challenge with respect to its thermal and emissive behavior. The scanning mechanism though aids in calibration by providing independent fore and aft looks. The radiometer incorporates special flight hardware which enables advanced Radio Frequency Interference (RFI) detection and mitigation in ground processing. Temporal and spectral bins which contain interference are discarded and the rest of the spectrogram is combined to form an uncalibrated measurement (Piepmeier et al, 2016). Periodic cold-sky maneuvers are performed which provide an independent point for evaluating relative and absolute calibration.

This paper covers the main features of the SMAP radiometer algorithm from  $T_A$  to  $T_B$ . This includes  $T_A$  forward models, antenna calibration method, radiometer internal calibration sources calibration, and results of calibration and validation activities. Section II covers the radiometer L1B algorithm to get the Earth's surface brightness temperature from RFI mitigated radiometer antenna temperature. Section III introduces the two  $T_A$  forward models used to generate expected antenna temperatures for calibration and validation. The radiometer pre-launch calibration method and results of the calibration/validation are described in Section IV. Summary of outstanding calibration issues and conclusions are discussed in Section V.

## II. LEVEL 1B ALGORITHM ( $T_A$ TO $T_B$ )

In order to go from  $T_A$  to  $T_B$ , we mostly rely on pre-launch or modeled values. Significant calibration factors such as backlobe spillover, internal calibration source, and Faraday rotation correction need external modeled calibration sources (e.g. cold-sky, Amazon, or Ocean) to compare measurements.

The flow of the  $T_A$  to  $T_B$  in the radiometer level 1B algorithm is shown in Figure 2.1. The input is the calibrated and RFI filtered antenna temperature ( $T_A$ ) and the output is the brightness temperature ( $T_B$ ) of the Earth's surface. There are three major correction algorithms: Antenna Pattern Correction (APC), Faraday rotation correction and atmospheric correction. The basis for these correction algorithms is described in (Piepmeier et al, 2016), and is outlined here to clarify the post-launch calibration algorithm.

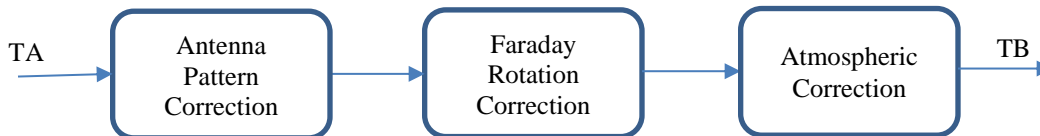


Figure 2.1: Diagram of the radiometer L1A/B correction algorithms

### 1. APC Correction

The APC algorithm flow is illustrated in Figure 2.2. This algorithm deconvolves sidelobes and removes cross-polarized contamination from the calibrated antenna temperature ( $T_A$ ) to produce the mainbeam-only apparent temperature at the top of ionosphere. During this process, the contributions from the Sun/Moon/galaxy are removed, and the correction due to reflector emissivity is also applied before the implementation of the Earth sidelobe correction.

The antenna temperature from the Earth surface is then given by

$$T_{A,earth} = T'_A - T_{A,DirSun} - T_{A,DirGal} - T_{A,RefSun} - T_{A,RefMoon} - T_{A,RefGal} \quad (2.1)$$

where  $T'_A$  is the antenna temperature after reflector emissivity correction.  $T_{A,DirSun}$  and  $T_{A,DirGal}$  are the antenna temperature directly from the Sun and the galaxy including the cosmic microwave background, respectively, while  $T_{A,RefSun}$ ,  $T_{A,RefMoon}$ , and  $T_{A,RefGal}$  are the antenna temperature after reflection off the Earth into the antenna from, respectively, the Sun, the Moon, and the galaxy.

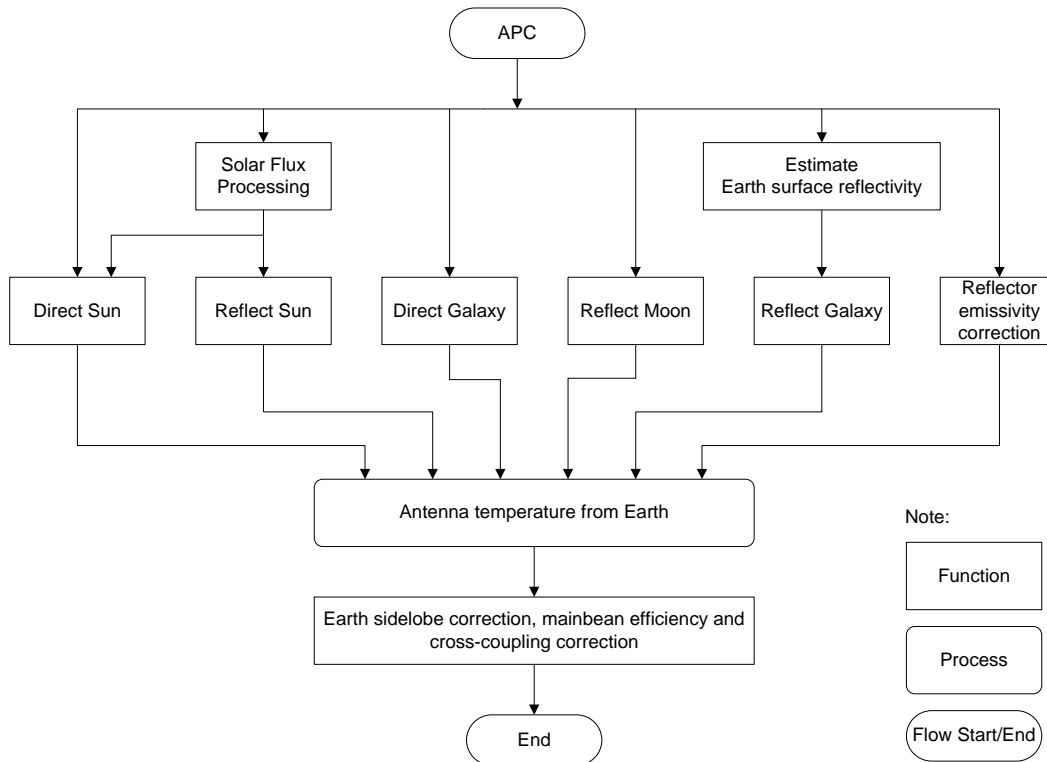


Figure 2.2. SMAP radiometer APC algorithm flow

In order to convert onto  $T_{A,earth}$  to obtain the apparent temperature at the top of ionosphere,  $T_{ap,toi}$ , a constant  $4 \times 4$  APC matrix derived from global simulations based on pre-launch models of the antenna pattern. Results from previous radiometers have shown that this transformation can be approximated quite well using the following matrix transformation (Dinnat et al, 2007; Meissner et al, 2010).

$$\begin{bmatrix} T_{ap,toi,v} \\ T_{ap,toi,h} \\ T_{ap,toi,3} \\ T_{ap,toi,4} \end{bmatrix} = M \cdot \begin{bmatrix} T_{A,earth,v} \\ T_{A,earth,h} \\ T_{A,earth,3} \\ T_{A,earth,4} \end{bmatrix} \quad (2.2)$$

## 2. Faraday Rotation Correction

Once the apparent temperature at the top of ionosphere is obtained, a Faraday rotation correction needs to be performed. Faraday rotation is a well-known phenomenon associated with wave propagation through an ionized medium subject to a stationary magnetic field, and the medium can alter the polarization state of the wave. L-band signals experience larger Faraday rotation relative to higher microwave frequencies. The amount of polarization rotation change can be expressed as

$$Q_{ap,toi} = \sqrt{(T_{ap,toi,v} - T_{ap,toi,h})^2 + T_{ap,toi,3}^2} \quad (2.3)$$

The Faraday rotation can be corrected by computing the apparent temperature at the top of atmosphere  $T_{ap,toa}$  from the  $T_{ap,toi}$  (Yueh, 2000).

$$\begin{bmatrix} T_{ap,toa,v} \\ T_{ap,toa,h} \\ T_{ap,toa,3} \\ T_{ap,toa,4} \end{bmatrix} = \begin{bmatrix} (T_{ap,toi,v} + T_{ap,toi,h} + Q_{ap,toi})/2 \\ (T_{ap,toi,v} + T_{ap,toi,h} - Q_{ap,toi})/2 \\ 0 \\ T_{ap,toi,4} \end{bmatrix} \quad (2.4)$$

A critical assumption for this correction is that the 3<sup>rd</sup> Stokes parameter from the Earth's surface is small.

## 3. Atmospheric Correction

At L-band, the atmospheric downwelling brightness is almost the same as the upwelling brightness. With this simplification, the atmospheric correction is given by

$$T_B = \frac{T_{surf}}{T_{surf} - T_{up}} \cdot [L \cdot T_{ap,toi} - (1 + L) \cdot T_{up}] \quad (2.5)$$

where  $T_B$  is the desired Earth surface brightness corrected for atmospheric effects.  $T_{surf}$  refers to the physical temperature at the bottom of the atmosphere near the Earth's surface for land and the SST for ocean. The atmospheric upwelling brightness,  $T_{up}$ , and total attenuation,  $L$ , are modeled in (Peng et al, 2013) and discussed in section III.

## III. TA FORWARD MODELS

The goal of the radiometer post-launch calibration is to adjust radiometer calibration factors (internal calibration sources, antenna pattern, etc.) by comparing radiometer measurements to modeled values over desired targets. The modeled values are generated by simulation. Considering the simulation speed, and visiting time and frequency over the calibration targets which

will be introduced in Section IV, two simulators are used. The first one is the detailed simulator which computes the antenna temperature using 2-D integration over all  $4\pi$  steradians of antenna pattern, and the second is the simplified version of the detailed simulator due to real-time simulation consideration.

### *1. Detailed simulator*

The detailed simulator is a forward algorithm to compute the antenna temperature with the given parameterized surrounding environment (the Earth's surface, atmosphere, ionosphere, the Sun/Moon/galaxy), and it is modified from the Aquarius simulator (LeVine et al, 2011) by adopting the SMAP specifications, such as its antenna pattern with narrower mainbeam, conical scan, etc. Efforts were spent on increasing the computational speed of the simulator including adding parallel-computing ability and using a simplified radiative transfer model (Peng et al, 2013) which is also used in the SMAP level 1B algorithm (Piepmeier et al).

For land surfaces, the Microwave Emission Model (MEM) (Njoku et al, 1999) with the Mironov dielectric model (Mironov et al, 2013) is used in the simulator. The land ancillary parameters include surface temperature, soil moisture, sand and clay fraction, open water fraction, vegetation water content and land roughness. The Earth's surface brightness temperature is computed at the top of the Earth's surface layer (e.g. vegetation) at a given incidence angle which depends on the relative position to the SMAP spacecraft. The brightness temperature for a given resolution cell, which size is determined by the antenna pointing direction and resolution, is the combination of TB from land and TB from water weighted by the water fraction.

Instead of being computed using the IRI-2000 model which is used in the Aquarius simulator, for SMAP the TEC data is directly downloaded from the International GNSS Service (IGS) (Schaer et al, 1998) and then it is used to compute the Faraday rotation angle in order to account for the Faraday rotation effect.

Due to multiple factors (program language, short radiometer integration time per measurement, limited computation resources, etc), the detailed simulator can't achieve real-time simulation with few computation cores. So the detailed simulator is only used for special cases that requires high precision and simulation fidelity, e.g., Cold Sky Calibration (CSC).

### *2. Simplified simulator*

The simplified simulator is used to compute the antenna temperature starting from the Earth's surface brightness temperature at the antenna boresight. The Land TB is derived from the Nature Run version 3 dataset (Reichle et al, 2014) if the land is in a non-freeze/thaw state; otherwise, fill values which signify no data are used. Similarly ocean TB is computed using the L-band Geophysical Model Function reported in (Yueh et al, 2013).

In general, the simulation in the simplified simulator is the inverse of the SMAP radiometer L1B algorithm from  $T_A$  to  $T_B$ , shown in Figures 2.1 and 2.2, except that the atmospheric radiative transfer model is slightly different and the Faraday rotation

angle is used to simulate the Faraday rotation effect.

Instead of functions of near surface air parameters (temperature, pressure, and water vapor density), the upwelling/downwelling brightness temperature and loss factor in the atmospheric radiative transfer model are, at a given incidence angle, functions of the Earth's surface elevation. At  $40^\circ$  incidence angle, the upwelling TB and loss factor are given by

$$T_{upwelling} = 0.0400H^2 - 0.5422H + 2.7755 \quad (2a)$$

$$L = 1.6495 \times 10^{-4}H^2 - 0.0021H + 1.0109 \quad (2b)$$

where  $H$  is the altitude of the earth surface in kilometer. For L-band emissions, the downwelling TB is nearly the same as the upwelling TB. The expressions of  $T_{upwelling}$  and  $L$  in Equation (2) were developed using the same radiosonde dataset as that used in (Peng et al, 2013). The atmospheric correction using Equation (2) has precision 0.069 K with assumption that the earth surface brightness is 242 K and the physical temperature of the Earth's surface is 300 K. The precision satisfies the requirement of 0.1 K error budget for the SMAP atmospheric correction.

The simplified simulator can achieve real-time simulation for each footprint in normal science mode. Simulation data is available if the SMAP radiometer is in normal science mode.

#### IV. CALIBRATION ALGORITHM, VALIDATION AND RESULTS

##### 1. Calibration algorithm and targets

###### a) Calibration using external targets

SMAP uses global ocean and Cold Sky (CS) measurements as its primary external references to refine pre-launch calibration coefficients including the APC matrix, similarly to the approach used for Aquarius (Dinnat et al, 2015). The global ocean, open water 200-km away from coastlines, are shown as blue in Figure 4.1a. Sea ice and heavy rain zone are excluded as well. The global ocean is used to identify any potential drifts in the calibration, and also aids in adjusting the corrections for extra-terrestrial error sources.

The CSC maneuvers involve pitching SMAP to observe the cosmic microwave background (CMB). CSC maneuvers are normally performed monthly with  $110^\circ$  pitch angle and an ocean background to minimize the backlobe uncertainty on predicted antenna temperatures. SMAP also performs a special CSC maneuver at  $180^\circ$  pitch angle with the backlobe observing a transition from ocean to Amazonian rain forest to provide information to refine the APC matrix.

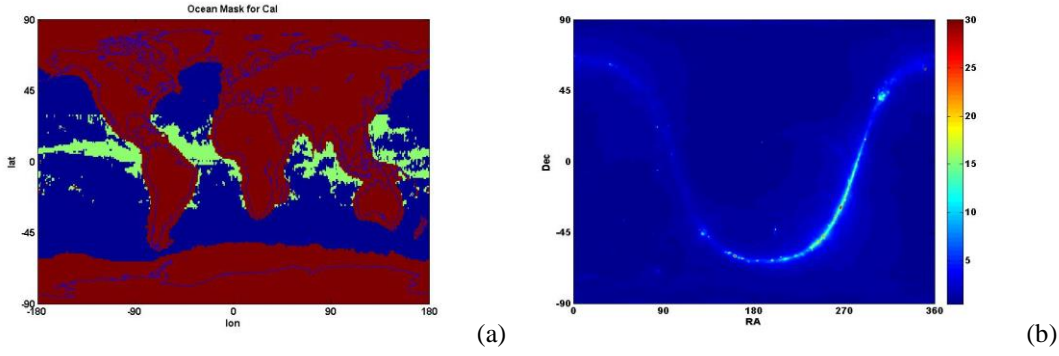


Figure 4.1: Calibration Targets for monitoring  $T_{ND}$  calibration bias and drift. (a) Global ocean mask in blue, heavy rain zone in green; (b) Map of celestial TB in equatorial coordinate system

The radiometer's calibration sources are adjusted if there is a bias between the radiometer measurements and the modeled values over desired targets. After the antenna pattern is calibrated by using the special CSC, the bias is assumed to be caused only by the uncertainty in the temperature of the noise diode ( $T_{ND}$ ), while the baseline values of the reflector and radome loss factor are used during this phase. Adjustment to  $T_{ND}$  could mitigate the bias and the adjustment is given by

$$\Delta T_{ND} = L_{RF}^{-1} \left( \frac{C_{ref+ND} - C_{ref}}{C_A - C_{ref}} \right) (T_{A,exp} - T_A) \quad (4.1)$$

where  $L_{RF}$  is the loss of the radiometer RF front end. Count values  $C_x$  ( $x = A, ref, ref+ND$ ) are the radiometer output counts for the antenna, reference load, and reference load with noise diode on states, respectively.  $T_{A,exp}$  is the modeled antenna temperature from the simulator, while  $T_A$  is the radiometer measurements.

#### b) Subband calibration

The SMAP radiometer provides science telemetry for the fullband channel (24 MHz wide) and 16 subband channels each 1.5 MHz wide. The radiometer has two operation modes (a high-rate mode and a low-rate mode) due to downlink data rate limitation. In high-rate mode both fullband and subband measurements are included in the telemetry. In low rate mode fullband data is always available while subband data is only available over land, coastal ocean and selected calibration/validation areas in the ocean. The reported  $T_A$  in the radiometer LIB data product is the mean of the RFI-free subband measurements if available; otherwise it is from the full band measurements. All of the fullband and subband measurements should therefore have the same calibrated TAs.

The fullband and subband channels can be calibrated using the above calibration approach with external calibration targets. For the 16 subbands, each of them can also be radiometrically calibrated with respect to the full band. The advantage of this subband calibration approach is that the fullband measurements always exist and they have full dynamic range which includes

the measurements over external calibration targets. The relation between the fullband measurement and subband measurements can be modeled as

$$T_{A,fb} = aT_{A,sb} + b \quad (4.2)$$

where  $T_{A,fb}$ ,  $T_{A,sb}$  are the antenna temperatures of the fullband and a single subband, respectively. The constants  $a$  and  $b$  are subband-dependent, and they can be estimated by

$$\bar{T}_{A,fb} = [\bar{T}_{A,sb} \quad I] \begin{bmatrix} a \\ b \end{bmatrix} \quad (4.3)$$

where  $\bar{T}_{A,fb}$ ,  $\bar{T}_{A,sb}$  are  $N \times 1$  vectors of the fullband and subband measurements, respectively.  $N$  is the number of measurements, and  $I$  is an  $N \times 1$  vector of number 1.

The constants  $a$  and  $b$  are estimated by computing the inverse of Equation (4.3), or

$$\begin{bmatrix} a \\ b \end{bmatrix} = (E^t E)^{-1} E^t \bar{T}_{A,fb} \quad (4.4)$$

where  $E = [\bar{T}_{A,sb} \quad I]$ , and the superscript  $t$  denotes matrix transpose.

The brightness temperatures of the subband calibration sources will be adjusted as

$$T'_{nd,sb} = aT_{nd,sb} \quad (4.5a)$$

$$T'_{ref,sb} = T_{ref,sb} + (a - 1)T_{ref,sb} + b \quad (4.5b)$$

where  $T_{nd,sb}$  and  $T'_{nd,sb}$  are the brightness temperatures of the subband noise diode before and after the adjustment, respectively.  $T_{ref,sb}$  and  $T'_{ref,sb}$  are the brightness temperatures of the subband reference load before and after the adjustment, respectively.

The radiometer measurements used in the subband calibration should be RFI-free and with antenna boresight or reflected antenna boresight off the Earth's surface away from the galactic plane. The requirement of RFI-free is due to that RFI signal is not wide band white Gaussian noise signal, and it might be strong beyond the linear range of the radiometer receiver. The other requirement is because of the neutral hydrogen (HI) which is abundant along the galactic plane, and the emission from HI has narrow bandwidth around 1.42 GHz (LeVine et al, 2004) which can also distort calibration.

## 2. Calibration and results

### a) Initial calibration to set $T_{nd}$ and $T_{ref}$

Before the reflector was deployed, the SMAP radiometer had been powered on with the feedhorn pointed to the Cold Sky. The internal noise diode was calibrated using CS for both the fullband and the subbands. The performance is described in (Piepmeier et al, 2015)

Figure 4.3 shows the difference between the fullband and subband  $T_A$ s after the reflector was deployed and fully spun-up, the subband  $T_A$ s are not the same as the fullband  $T_A$ , and their difference is shown in blue in Figure 4.3. The difference might be due to two factors: 1) The mainbeam efficiency of the antenna is frequency-dependent. At lower frequency, the antenna mainbeam is wider so that its mainbeam efficiency is lower; 2) there might be standing wave between the reflector and the radiometer receiver since the  $T_A$  difference vs subband index presents a sinusoidal behavior.

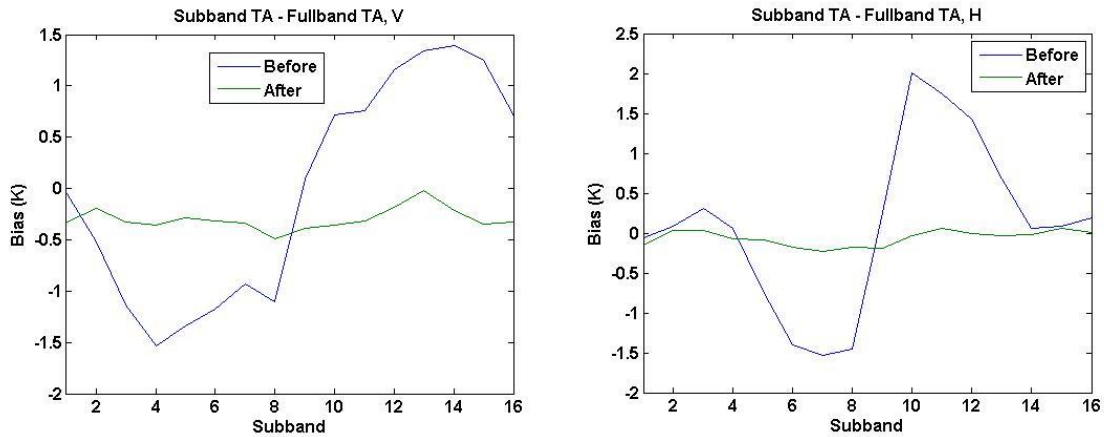


Figure 4.3  $T_A$  difference between subbands and fullband  $T_A$ s. (blue) before and (green) after subband calibration adjustment.

(left) V-pol; (right) H-pol

The subband calibration described in Section 4.1.b was applied after the reflector deployment. The values of the constants  $a$  and  $b$  for all of the subbands are shown in Figure 4.4. The  $T_A$  differences between the subbands and the fullband shown in green in Figure 4.3 are reduced significantly.

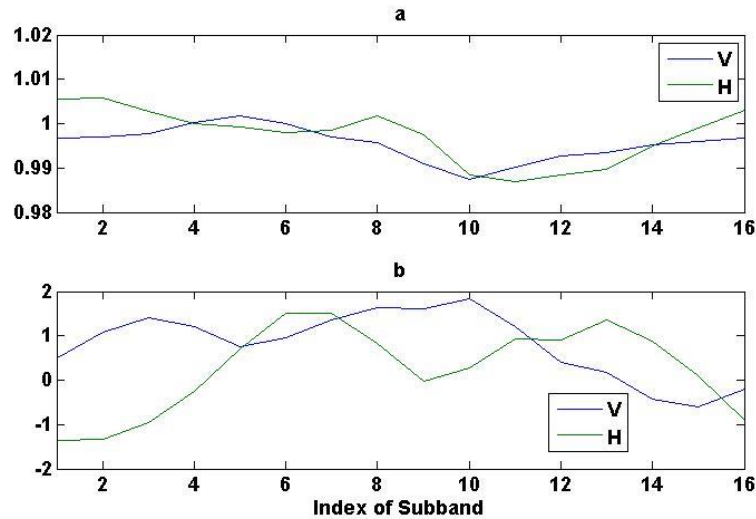


Figure 4.4 Subband calibration coefficients.

#### b) Geolocation assessment

The accuracy of the geolocation in the reported radiometer L1B dataset was computed prior to all of the radiometer electronic calibration, since the expected antenna temperature is computed (or selected) based on the reported geolocation of its corresponding footprint. SMAP requires footprint geolocation knowledge uncertainty of less than 4 km in the L1B data product. The accuracy of the geolocation data was verified via a comparison of the reported geolocation of the instrument's footprints against the radiometric antenna (or brightness) temperature data at and near straight coastlines (at the spatial resolution of the footprint) and free of near-shore islands or lakes/ivers. Antenna temperatures undergo a quick change as a reasonably symmetric antenna scans across coastlines which represent a high-contrast scene. The change corresponds to the convolution of the antenna pattern with a step function, which is mathematically represented as a sigmoid curve (Moradi et al, 51; Poe et al, 2008; Purdy et al, 2006; Wiebe et al, 2008). The midpoint of the sigmoid represents both the largest gradient in temperature and the location of the land/water boundary, and the location (latitude/longitude) is determined from the Global Self-consistent Hierarchical High-resolution Shoreline (GSHHS) map with 40-meter resolution (Wessel et al, 1996). The uncertainty is then obtained by comparing the location to the reported location in the L1B data file.

The selected coastlines and 13 half-orbits for geolocation assessment are shown in Figure 4.5. The common characteristic among these 13 orbits is a near-perpendicular or near-parallel direction of the satellite ground track with respect to the coastline.

This ensures that either the edge or the central part of the swath crosses perpendicular to the geographical coastline during the antenna azimuthal scan. The average uncertainty of all detections is 2.7 km after applying a 0.13 degree counterclockwise yaw correction – a remarkably small error (less than 7% of footprint size) that can be considered the theoretically achievable limit by the algorithm on the SMAP footprint.

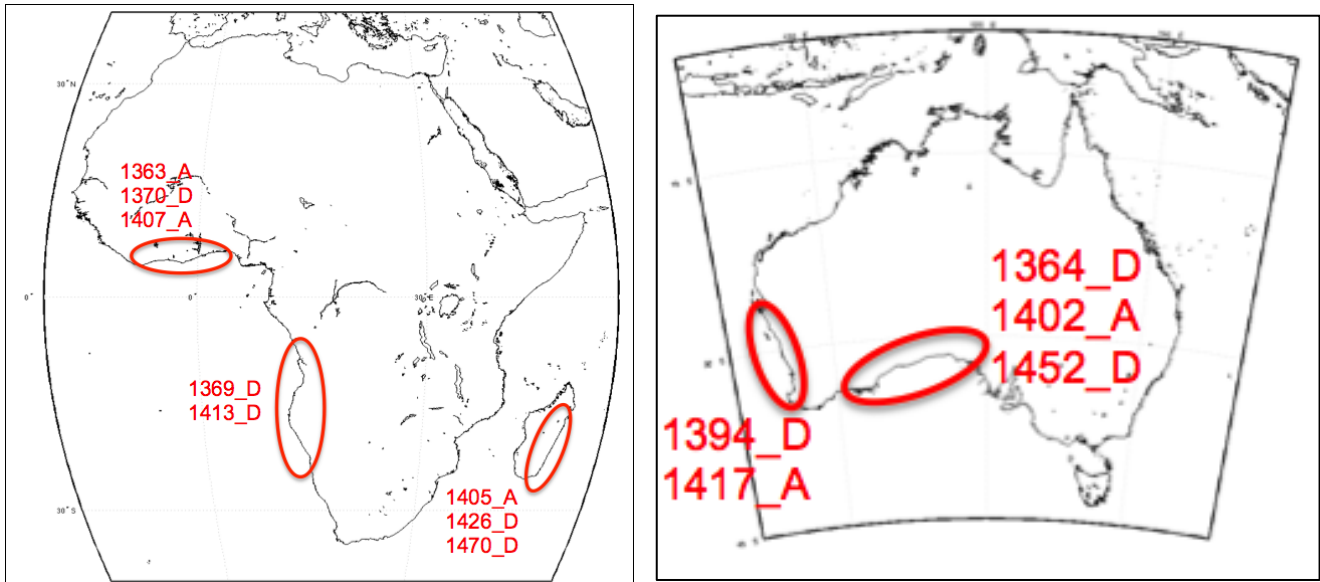


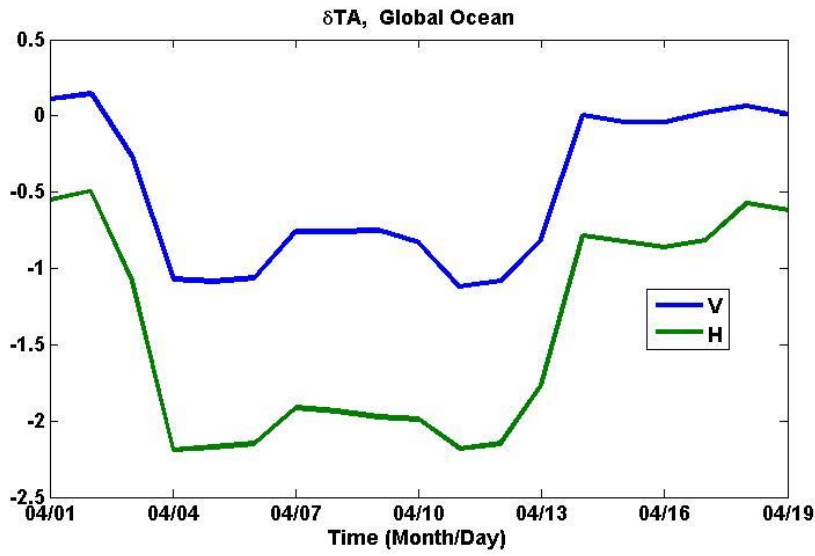
Figure 4.5: The selected half-orbits with ground tracks either near-perpendicular or near-parallel to geographical coastlines.

### c) Front-end loss calibration

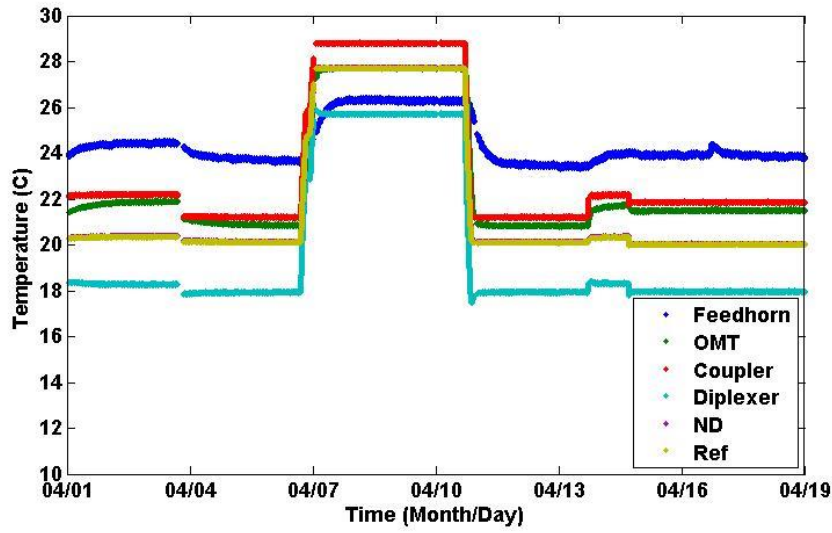
Besides the input signal, a microwave radiometer is also sensitive to its physical temperature change. The front-end loss calibration compensates for the  $T_A$  change due to the variation of the physical temperature of the radiometer RF front-end. Figure 4.6(b) shows the RF element temperatures during a planned bake-out. Before bake-out the SAR transmitter was also turned off. The global  $\delta T_A$  (Figure 4.6(b)) over the ocean shows two separate impacts due to these events.

- 1) A drop in the measured  $T_A$  with respect to the modeled  $T_A$  when the SAR transmitter was turned off, and
- 2) A rise in the measured  $T_A$  with respect to the modeled  $T_A$  when the RF bake-out was occurring.

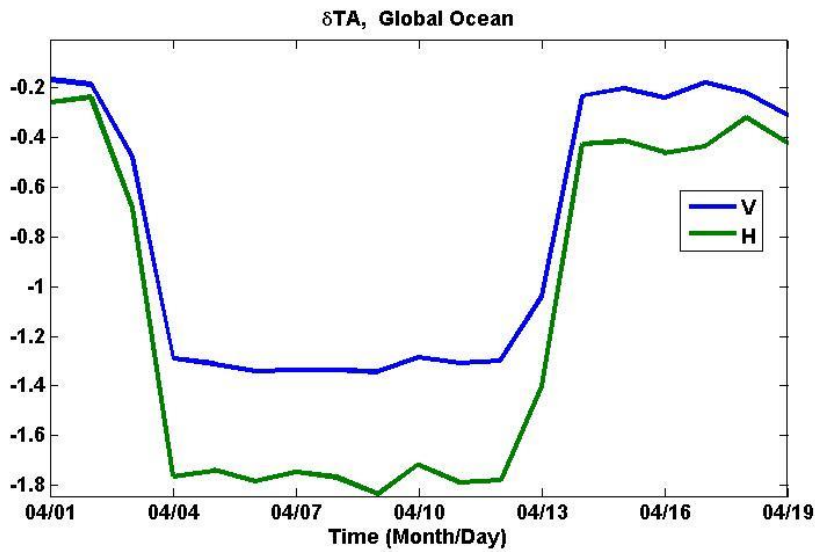
The  $T_A$  bias due to the SAR transmitter being turned off is an expected occurrence from pre-launch data analysis. The radiometer data calibration parameters have been set based on the SAR transmitter being turned on. On July 7, 2015 (not shown in Figure 4.6), the SAR transmitter encountered an anomaly that turned off the radar, causing a shift in radiometer calibration. The data compensates for this anomaly by adjusting the  $T_{ND}$  values to account for the offset bias. The result is shown in Figure 4.11 (b).



(a)



(b)



(c)

Figure 4.6: (a) Daily averaged global ocean  $\delta T_A$  indicating  $T_A$  biases due to SAR transmitter being turned off (Apr 3, 2015) and on (Apr 13, 2015) and radiometer bake-out (Apr 6 to Apr 10, 2015). (b) Front-end temperature of the RF components over the same period. (c) Daily averaged global ocean  $\delta T_A$  indicating  $T_A$  biases during bake-out after the adjustment of the RF front-end thermal coefficients.

The second front-end impact observed from Figure 4.6 is the change in  $T_A$  bias with change in the RF temperature components. The RF front-end thermal calibration coefficients cannot completely compensate for the changing thermal environment of the RF components. Thermal coefficients to the RF front-end parts are adjusted to compensate the impact of this event. The result of this update is shown in Figure 4.6(c).

#### d) Antenna pattern calibration

A special CSC designed to assess the uncertainty on the antenna pattern was conducted on Jun 22, 2015 with the spacecraft flying over a transition between ocean and land (Amazonian rain forest, Figure 4.7) pitched at  $180^\circ$ . The observation over the transition from ocean to land is shown in Figure 4.8(a). The CSC uses the very large contrast in  $T_B$  between water and land to assess the fraction of antenna power pointing toward the Earth. The difference (or  $\delta T_A = T_A - T_{A,exp}$ ) of V-pol between the observation and the model is shown in Figure 4.8(b). From ocean to land, the  $\delta T_A$  is changed  $-0.63$  K and  $-0.43$  K for V and H polarizations, respectively. This is due to the uncertainty in the modeled antenna pattern. Scaling factors are applied to antenna pattern with 0.967 for V-pol and 0.948 for H-pol to the antenna backlobe, and 1.0027 for V-pol and 1.0042 for H-pol to the rest part of the antenna pattern. The purpose of this correction is to keep  $\delta T_A$  unchanged during ocean-land crossing.

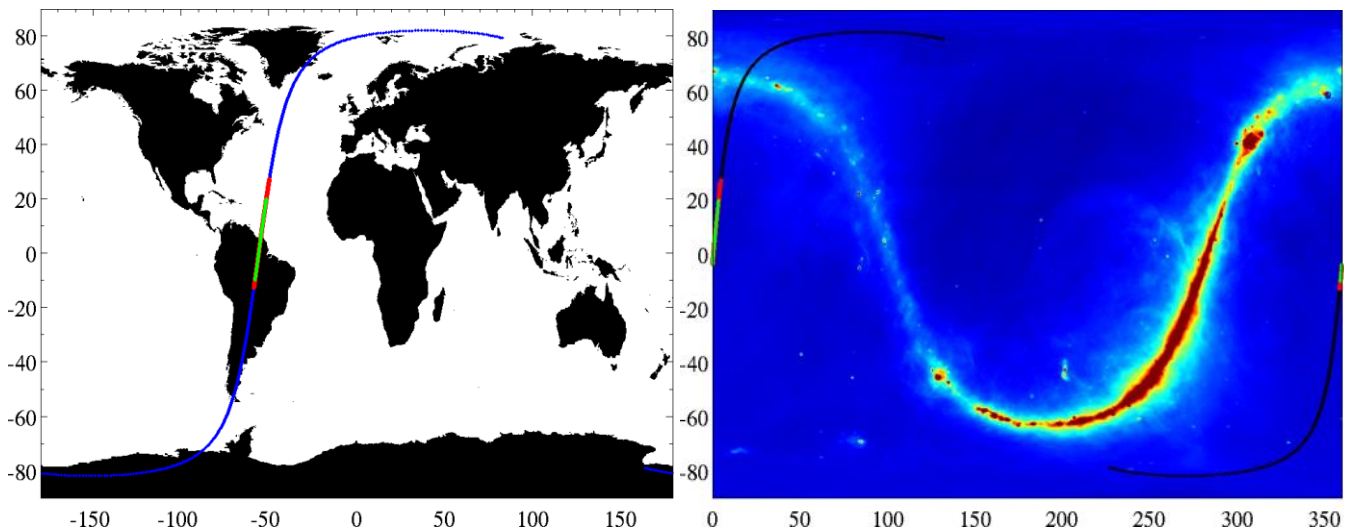


Figure 4.7: SMAP spacecraft ground track over the Earth (left) and the celestial sky (right, color map reports the cold sky  $T_B$ ) for the ocean-land crossing CSC on Jun 22, 2015.

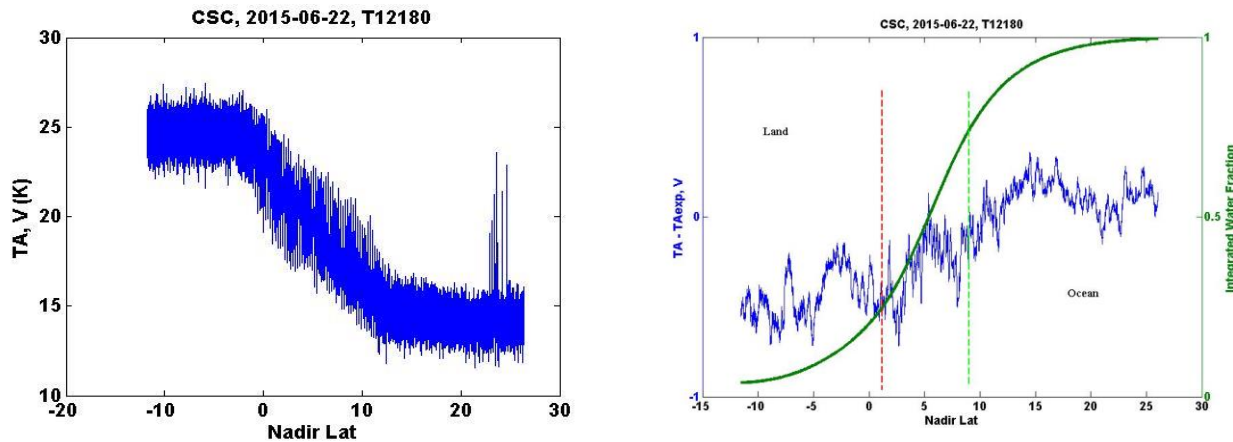


Figure 4.8: (left) SMAP observations over a transition between ocean and land. (right) The difference between the observation and the model over the transition from ocean to land is reported in blue. Integrated Water Fraction (IWF) defined as the integration of water fraction on the Earth's surface over the Visible Disk (the portion of antenna pattern intercepted by the Earth), or  $\int_{VD} w_f d\Omega / \int_{VD} d\Omega$ , is in green. Land region is with  $IWF < 0.25$  and ocean region is with  $IWF > 0.75$ .

In addition to the antenna pattern being calibrated by using the special CSC, it is also adjusted by considering the scanning effect which can be distinguished by comparing the two antenna pattern shown in Figure 4.9. The left plot is of the instantaneous antenna pattern, while the right one is of the effective antenna pattern obtained by integrating the instantaneous antenna pattern over one footprint scanning (approximately equivalent to  $1.2^\circ$  scan angle). With this consideration, the change of the gain matrix (or Stokes vector in (Piepmeier et al, 2008) integrated within the antenna mainbeam) is given by

$$M_{I2E} = \begin{bmatrix} 1.0002 & 0 & 0.0002 & 0 \\ 0 & 1.0006 & 0.0001 & -0.0001 \\ 0.0002 & 0.0005 & 1.0011 & -0.0003 \\ -0.0001 & 0 & 0.0005 & 1.0011 \end{bmatrix} \quad (4.2)$$

The product of Equation (4.2) and the results from the special CSC gives

$$M_{adjust} = M_{I2E} M_{SCSC} = \begin{bmatrix} 1.0029 & 0 & 0.0002 & 0 \\ 0 & 1.0048 & 0.0001 & -0.0001 \\ 0.0002 & 0.0005 & 1.0046 & -0.0004 \\ -0.0001 & 0 & 0.0005 & 1.0046 \end{bmatrix} \quad (4.3)$$

where  $M_{SCSC}$  is the scaling matrix from the special CSC, and it is given by

$$M_{SCSC} = \begin{bmatrix} 1.0027 & 0 & 0 & 0 \\ 0 & 1.0042 & 0 & 0 \\ 0 & 0 & 1.0034 & 0 \\ 0 & 0 & 0 & 1.0034 \end{bmatrix} \quad (4.4)$$

The inversion of the matrix  $M_{adjust}$  is applied onto the APC matrix  $M$  in Equation (2.2).

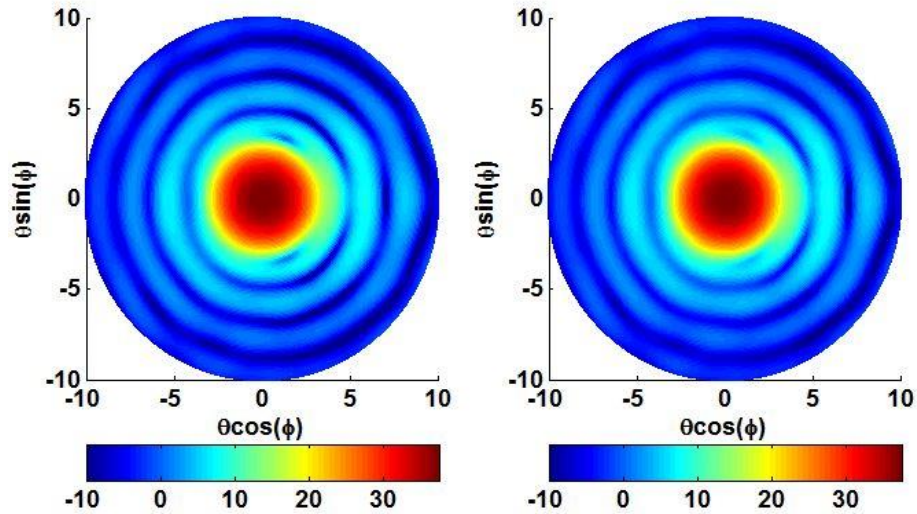


Figure 4.9 Instantaneous V-pol antenna pattern (left), and effective V-pol antenna pattern (right) considering scanning effect over  $1.2^\circ$ .

#### e) Drift and bias removal

After the radiometer was powered on, global ocean (Figure 4.1, blue portion) has been used as an external target to monitor calibration bias and drift in  $T_{ND}$ .

It was observed that the measured  $T_A$ 's were drifting comparing to the ocean L-band GMF model (Yueh et al., 2013). Besides drift, there were also biases, which were likely due in part to standing wave between the reflector and radiometer front end, and error in antenna pattern. The drift and bias from Apr 1 to Jun 22, 2015 are shown in Figure 4.10, where  $\delta T_A (= \langle T_{A,measured} - T_{A,model} \rangle_{day})$  are the daily averaged differences between measured and expected antenna temperatures. The biases on Apr 1, 2015 are 0.11 K and -0.55 K for V- and H-pol measurements, respectively. The difference,  $\delta T_A$ , had been drifting at an almost constant rate before May 27, 2015, and then became constant, indicating that the radiometer is stable (at least temporarily).

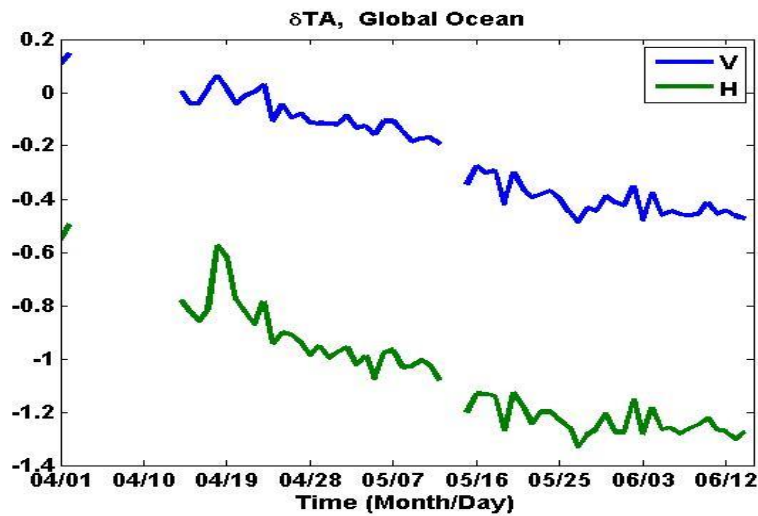
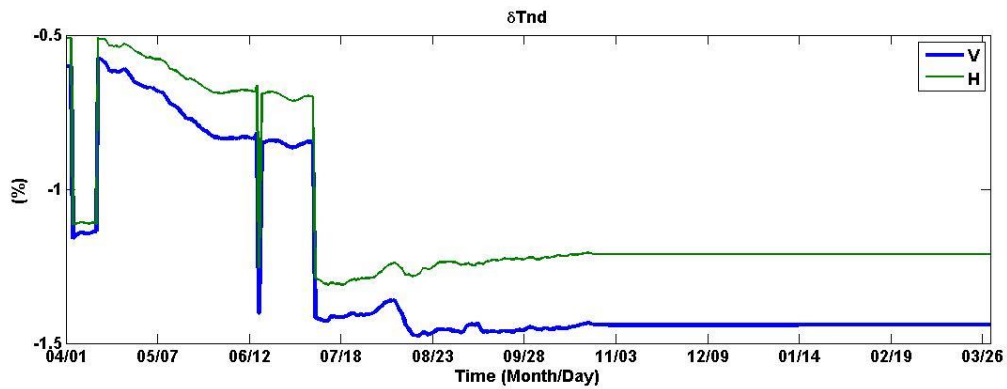


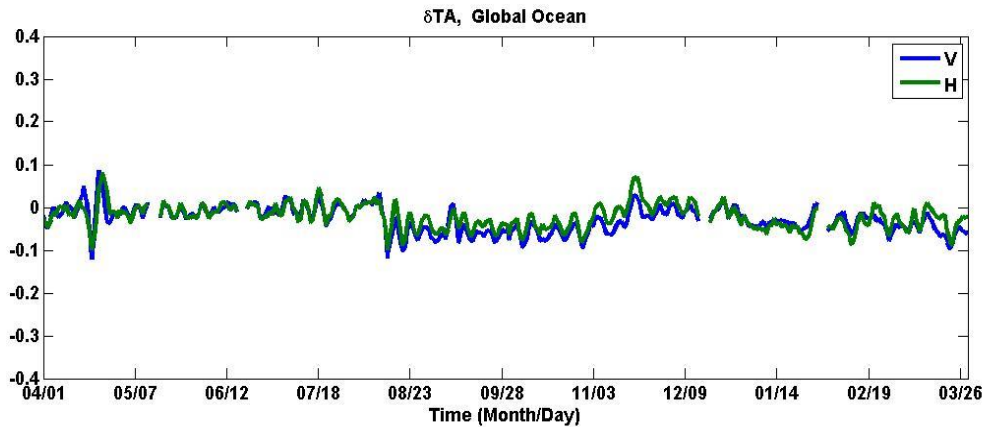
Figure 4.10: Radiometer  $T_A$  calibration bias and drift between April 1 and June 22 of 2015. Note: data is not shown during bake-out and SAR transmitter off period

It was also observed that the measured  $T_A$  dropped about 1.1 K for V-pol and 1.3 K for H-pol when the radar transmitter was off (2 times powered-down before July 7, 2015 and permanent failure thereafter) which leads to that the physical temperature of the radiometer decreased and eventually stabilized at a new plateau. Even though the sensitivity of the calibration to the physical temperature of the radiometer is considered in the antenna temperature calibration, The drops in  $T_A$  is likely due to the changes in the thermal gradients of the noise diode which has much larger temperature sensitivity than other RF components.

In order to remove the drift or time-varying bias, the approach described in Section IV.1 is used to update  $T_{ND}$  daily if drift/bias exists or at the start time (resolution in minutes) of the half orbit with SAR transmitter on/off. A linear interpolation is applied to derive  $\delta T_A$  for daily data without enough data samples. Daily updated  $T_{ND}$  before November 01, 2015 is then smoothed by 8-day averaging and used for L1A data processing to get L1B data. The  $T_{ND}$  bias due to SAR transmitter on/off is compensated before the 8-day averaging is applied, and the bias is added back after the averaging. The percentage of the  $T_{ND}$  adjustment is shown in Figure 4.11(a) and the residual drift/bias is shown in Figure 4.11(b). The residual bias and precision of the calibrated  $T_A$  during the first year of the SMAP mission are all less than 0.03 K for both V and H channels. Note: These results include the results of the front-end loss calibration discussed in Section IV.2.c and the antenna pattern calibration with SCS in Section IV.2.d.



(a)



(b)

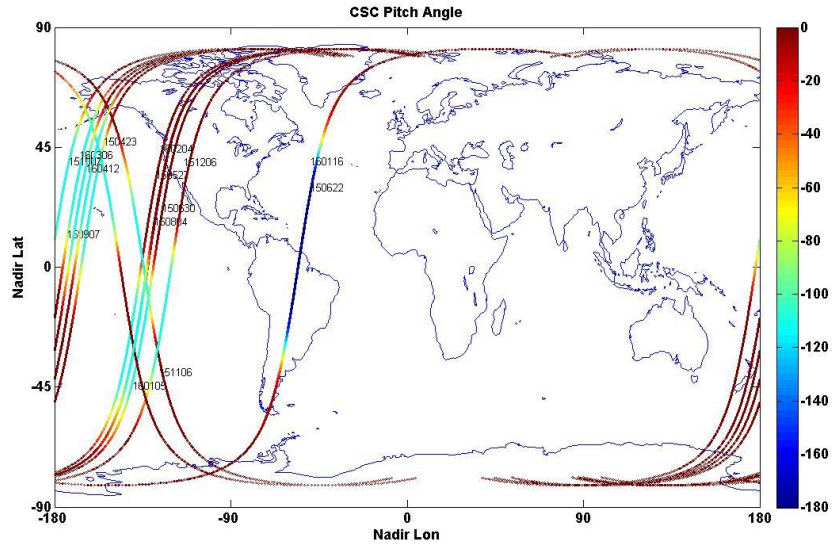
Figure 4.11: Radiometer  $T_A$  calibration bias and drift correction. (a)  $T_{ND}$  change in percentage; (b) residual  $T_A$  drift/bias in Kelvin for (blue) V- and (green) H-pol.

### 3. Validation and result

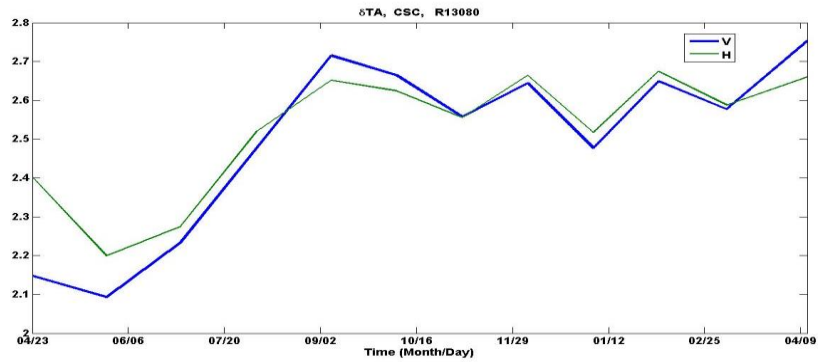
#### a) Validation over normal CS

The celestial sky at L-band (Figure 4.17, right panel) is used for the post-launch empirical calibration of the radiometer because it offers well-characterized  $T_B$ , spatial homogeneity over large regions and very high temporal stability. It is also free of RFI. Normal CSC (110° pitch angle) has been used to determine the instrument bias and its stability in time.

In general, normal CSC is performed monthly with the spacecraft above open-ocean to limit uncertainty due to the land emission model (Figure 4.12(a)). The  $T_A$  drift during the first year since April, 2015 is shown in Figure 4.12(b). Besides the drift over time, there are biases in both V and H channels, most likely due to uncorrected reflector/radome losses and the offset in reference load.



(a)



(b)

Figure 4.12: (a) SMAP spacecraft ground track over the Earth with pitch angle reported in the colorbar and time (YYMMDD).

(b)  $T_A$  drift over CS.

### b) Reflected galactic correction assessment

During the cal/val period, the map of the radio galaxy used for estimating the contribution of reflection of the galaxy off the Earth's surface and into the antenna mainbeam has been modeled as the convolution of the Sky TB map with a circularly symmetric averaged beam pattern. This is further convolved with the smearing introduced by a 7-m/s wind over the ocean surface. The net effect is equivalent to a smoothed (lacking all bumps and local maxima/minima of the true beam pattern) and wider (about 1.3 times larger half-power-beam-width) antenna mainbeam.

Figure 4.13 shows the result of the reflected galaxy correction in  $T_B$  (V-pol here) using a representative set of consecutive descending orbits. The data are segregated by the antenna scan angle, which indicates whether the instrument is pointing forward

or backward with respect to the orbital velocity vector, and binned on a 0.25-deg grid. Within each grid cell the data are weighted by the inverse of their distance to the center of the grid cell.

The stripes along the ground tracks of the orbits are caused by the reflection of the galaxy into the main antenna beam (over land, it might due to geography; in the high southern latitudes near Antarctica it is due to sea ice boundaries.). Under appropriate conditions of time-of-day illumination, and reflecting angle, the difference between TBs of a pixel as seen in a forward or backward look reaches up to 1 K over ocean (smaller over land due to smaller land reflectivity in general).

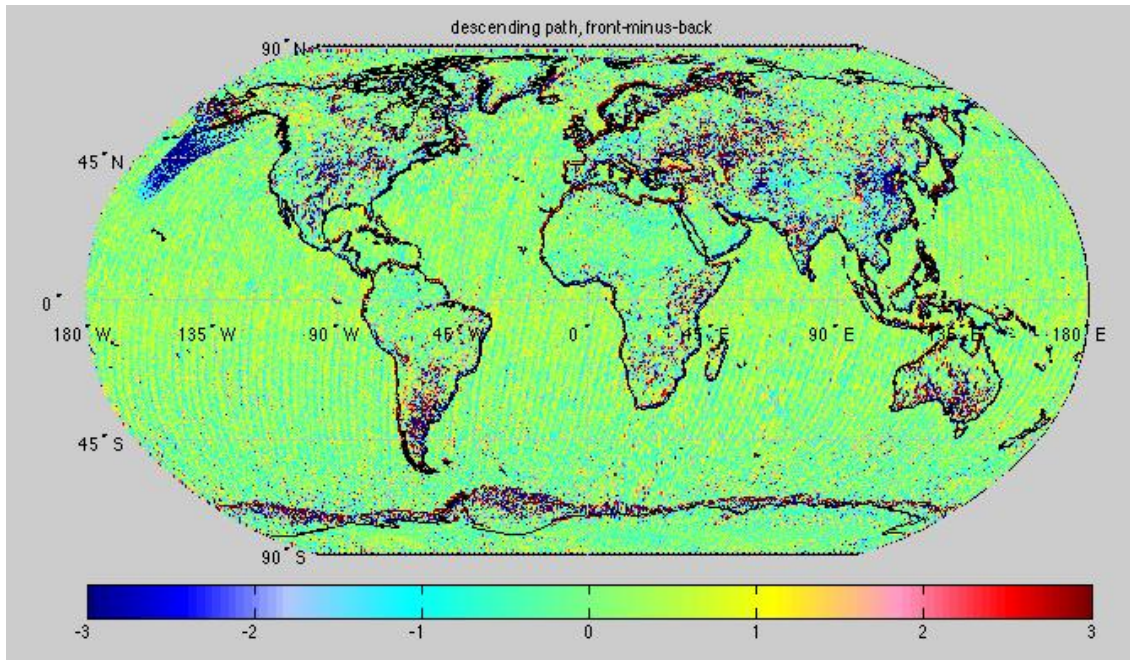


Figure 4.13: The descending  $T_B$  (V-pol) data for days 20150411-to-20150420, Data are segregated by forward/backward respect to orbital motion, and then averaged in 0.25-degree bins. The difference between the forward-looking data and the backward-looking data is used to eliminate the DC component of any signal and to highlight differences.

### c) Uncertainty over global ocean

Ocean is a relatively well-known and well-modeled target, and the brightness temperature variation within a footprint or among adjacent footprints over ocean is much smaller than that over land. Due to this, global ocean is used as the target to assess the uncertainty in the L1B\_TB.

For the radiometer, this science requirement for radiometric uncertainty is  $< 1.3$  K (with fore and aft averaging) over land. The equivalent requirement is  $< 1.8$  K on L1B TB basis, and  $< 1.6$  K on L1B  $T_A$  considering that the antenna mainbeam efficiency is about 90%.

Ocean has a smaller TB compared to land. The equivalent requirement can be scaled according to the ocean TB and it gives < 1.4 K over ocean on L1B land TB basis. Eight days' data (May 01~08, 2015) are used to assess the uncertainty in SMAP L1B\_TB. The uncertainty (rms) is not larger than 1.2 K for both V and H pols.

## V. CONCLUSION/DISCUSSION

This paper provides the analysis and assessment of the calibration quality of SMAP radiometer brightness temperatures available in the L1B\_TB data products (Composite Release Identifier, or CRID: R13080). Calibration methods include Cold Sky and vicarious ocean calibration with effective antenna pattern considered. Calibration stability and quality are assessed using global ocean and Cold Sky targets and geolocation is verified using conventional coastal-crossing analysis.

The instrument is performing as expected. Both geolocation accuracy and radiometric uncertainty meet the project requirements. Results show the geolocation performance meets the requirements with ample margin. The radiometer drift is monitored daily using the global ocean and monthly using the Cold Sky. Currently, the drift is corrected by adjusting noise diode calibration coefficients since the noise diode's brightness temperature has the largest uncertainty. This results in both the calibration drift and calibration bias over ocean not being larger than 0.03 K in the first year on orbit. However, there is bias and drift over the Cold Sky, and it shows that radome/reflector correction is necessary with the updated reflector thermal model. Due to the high correlation between reflector and radome temperature changes, further analysis is required to assign a calibration correction to the front-end loss elements. The radome and reflector temperatures are also orbit- and latitude-dependent, potentially causing geographic ocean  $T_A$  biases to get aliased into the analysis. These factors must be considered before applying a radome/reflector correction.

The correction for the reflected galaxy is assessed by using the fore/aft difference over ocean. Results show that it still requires further improvement. One such improvement could be the indexing of the effective beam pattern profile by the clock angle of the scan, while concurrently using the asymmetric 'real' beam pattern for the convolution with the wind speed and galactic signal. A further step could be to modify the surface reflectivity to account for varying wind speed. Alternative approaches are under consideration and will be further explored.

## REFERENCES

- Dinnat et al. (2007). Effects of the Antenna Aperture on Remote Sensing of Sea Surface Salinity at L-Band. *IEEE Trans. Geosci. Remote Sens.*, 45(7), 2051 - 2060.

- Entekhabi et al. (2010, May). The Soil Moisture Active Passive (SMAP) Mission. *Proceedings of the IEEE*, 704-716.
- LeVine et al. (2004). Galactic Noise and Passive Microwave Remote Sensing From Space at L-Band. *IEEE Trans. Geosci. Remote Sens.*, 42(1), 119 - 129.
- LeVine et al. (2011). The Aquarius Simulator and Cold-Sky Calibration. *IEEE Trans. Geosci. Remote Sens.*
- Meissner et al. (2010). *GMI Calibration Algorithm and Analysis Theoretical Basis Document, version E*. Santa Rosa: Remote Sensing Systems.
- Mironov et al. (2013). Temperature- and Texture-Dependent Dielectric Model for Moist Soils at 1.4 GHz. *IEEE Geosci. Rem. Sens. Ltrs.*, 10(3), 419~423.
- Moradi et al. (51). Correcting Geolocation Errors for Microwave Instruments aboard NOAA Satellites. *IEEE TGRS*, 3625.
- Njoku et al. (1999). Retrieval of land surface parameters using passive microwave measurements at 6-18 GHz. *IEEE Trans. Geosci. Remote Sens.*, 37(1).
- Peng et al. (2013). Global Simplified Atmospheric Radiative Transfer Model at L-Band. *IEEE Geoosci. Rem. Sens. Ltrs.*, 10(3), 437~440.
- Piepmeier et al. (2008). Stokes Antenna Temperatures. *IEEE Trans. Geos. and Remote Sens.*, 46(2), 516-527.
- Piepmeier et al. (2015). *SMAP Radiometer Brightness Temperature Calibration for the LIB\_TB and LIC\_TB Beta-Level Data Products*.
- Piepmeier et al. (n.d.). *SMAP LIB Radiometer Time-Ordered Brightness Temperatures*. Boulder, Colorado USA: NASA National Snow and Ice Data Center Distributed Active Archive Center.
- Poe et al. (2008). Geolocation error analysis of the special sensor microwave imager/sounder. *IEEE TGRS*, 913~922.
- Purdy et al. (2006). Geolocation and pointing accuracy analysis for the WindSat sensor. *IEEE TGRS*, 496~505.
- Reichle et al. (2014). *The SMAP\_Nature\_v03 Data Product*. NASA.
- Schaer et al. (1998). *IONEX: The IONosphere Map EXchange Format Version 1*. GPS-IONO.
- Wessel et al. (1996). A Global Self-consistent, Hierarchical, High-resolution Shoreline Database. *J. Geophys. Res.*(101, #B4), 8741-8743.
- Wiebe et al. (2008). Geolocation of AMSR-E data. *IEEE TGRS*, 3098~3103.
- Yueh et al. (2013). L-Band Passive and Active Microwave Geophysical Model Functions of Ocean Surface Winds and Applications to Aquarius Retrieval. *Geoscience and Remote Sensing, IEEE Transactions on*, 51(9), 4619~4632.
- Yueh, S. H. (2000). Estimates of Faraday Rotation With Passive Microwave Polarimetry for Microwave Remote Sensing of Earth Surfaces. *IEEE Trans. Geosci. Remote Sens.*, 38(5).